processes

MDPI

Article

Wellbore Stability Analysis of Shale Formation Considering Sealing Effect of Mud Cake on Drilling Fluid Seepage

Qiang Gao [1,*], Yun Bai [1], Shuaizhi Ji [1], Junying Zhang [1], Shitian Wan [1], Hongxia He [1], Feng Huang [1], Junling Lou [1] and Qiang Li [2]

[1] Technical Monitoring Center, China Petroleum and Chemical Corporation Limited Zhongyuan Oilfield Company, Puyang 457001, China; baiy.zyyt@sinopec.com (Y.B.); jiszjczx.zyyt@sinopec.com (S.J.); jyzhang_sinopec@126.com (J.Z.); wansht.zyyt@sinopec.com (S.W.); hongxiahe_sinopec@126.com (H.H.); fenghuang_sinopec@126.com (F.H.); jllou_sinopec@126.com (J.L.)

[2] Faculty of Engineering, China University of Petroleum-Beijing at Karamay, Karamay 834000, China; liqiang202403@cupk.edu.cn

* Correspondence: gqiang.zyyt@sinopec.com

Abstract

Wellbore stability is one of the major challenges during drilling operations in shale gas formations. Drilling fluid seepage can significantly alter the pore pressure around the wellbore, thereby inducing wellbore instability. In this study, the Darcy pore fluid flow model was applied to both the mud cake and wellbore to predict pore pressure, which helps improve the accuracy of calculating collapse pressure and fracture pressure. Shale samples were collected from the Puguang Gas Reservoir, and their composition and physicochemical properties were systematically analyzed. The results indicate that the clay content in the formation can reach up to 35.5%, with distinct hydrophilic characteristics, and the maximum hydration expansion rate of the shale is 5.79%. The permeabilities of shale and mud cake were measured via the pore pressure transmission test. Specifically, shale samples from Sub-layer 1 exhibit the highest permeabilities for both rock and mud cake, which are 8.27×10^{-18} m^2 and 2.07×10^{-20} m^2, respectively. In contrast, samples from Sub-layer 3 show the lowest permeability values, being 2.76×10^{-20} m^2 and 1.66×10^{-22} m^2. The borehole tensile breakdown pressure and compressive collapse pressure were calculated using a poro-mechanical coupling model. The Sub-layer with the lowest cohesion strength after drilling fluid immersion presents the narrowest mud density window of 0.04 g/cm^3, making it the most susceptible to wellbore stability failures; furthermore, the maintenance of wellbore stability requires strict control of the drilling mud density within the range. This study can provide guidance for accurate prediction of mud density window during drilling operations in shale formations.

Keywords: wellbore stability; pore fluid seepage; mud cake; safe drilling mud density window

Check for updates

Academic Editor: Qingbang Meng

Received: 28 February 2026
Revised: 12 March 2026
Accepted: 18 March 2026
Published: 21 March 2026

1. Introduction

Shale gas reservoirs have attracted considerable attention over the past decades and account for a substantial proportion of the global oil and gas energy supply [1–4]. However, during the drilling of long horizontal shale gas wells, wellbore instability has become a critical factor that prolongs operational time and increases overall project costs [5–10]. Shale reservoirs exhibit extremely low permeability, and the seepage of pore fluids in wellbore rocks, with the induced variations in the effective stress field in the near-wellbore zone, poses a major challenge to the accurate prediction of borehole fracture and collapse

https://doi.org/10.3390/pr14061002

pressures [1–4,11], which are two key parameters that exert a significant influence on the wellbore stability of horizontal shale gas wells [12].

To mitigate drilling fluid seepage, plugging materials such as asphalt, resin-based composites, polymers, and nanomaterials [13–19] are employed to form a dense mud cake that blocks filtration channels and reduces pore pressure transmission. Scholars have developed coupling models to investigate the influence of mud cake on borehole instability [11,20–22]. Tran et al. [11] derived analytical solutions for mud cake accumulation, and further studied the effects of mud cake properties on formation pore pressure and wellbore stress, as well as their subsequent impacts on the safe drilling fluid density window. The research results indicated that lower mud cake permeability can expand the safe drilling fluid density window. The permeability of mud cake is a non-negligible factor and neglecting it will lead to overestimation of the window range. Feng et al. [23,24] proposed a numerical method and adopted the equivalent mud cake filtration model to evaluate the effects of mud cake thickness and permeability reduction on wellbore surrounding stress fields. Rudyak and Seryakov [25] considered both uniform and non-uniform mud cake distributions and realized reasonable interpretation of logging data. Li et al. [26] and Zhang et al. [27] incorporated the time-dependent characteristics of mud cake into the hydro-mechanical model. By introducing the influence of mud cake permeability on pore fluid flow and wellbore stress, the prediction accuracy of the safe drilling mud density window was further improved. Wan et al. [28] and Zhang et al. [29] investigated the effects of mud cake on fracture internal pressure, and their results indicated that lower mud cake permeability corresponds to better performance of lost circulation materials in inhibiting fracture propagation. In the aforementioned models, mud cake thickness and permeability were taken as known parameters for sensitivity analysis. However, how these parameters can be obtained based on fluid flow models and incorporate them into hydro-mechanical models to predict wellbore collapse pressure or fracture pressure has rarely been reported.

In this study, shale samples were collected from the Qianfoya Formation of Puguang Gas Reservoir, where widespread oil and gas indications and high organic matter abundance have been identified, indicating promising development potential. As reported by Gao et al. [30] and Bo et al. [31], severe borehole collapse occurred in the Qianfoya Formation shale interval of the horizontal section, resulting in a total backfilling footage of 5361 m and a total complex operation period of 372 days, which caused substantial economic and time efficiency losses. A series of systematic laboratory tests were conducted to characterize their chemical composition and physical properties for wellbore stability analysis. A pore fluid flow model that considers both the mud cake and shale formation was adopted. Mud cake thickness and permeability, as well as shale permeability, were determined by fitting the experimental data from pore pressure transmission tests with the model. Based on a hydro-mechanical coupling model, the wellbore pore pressure distribution was obtained and wellbore stability analysis was performed to predict the compressive collapse pressures and tensile fracture. The results can serve as a theoretical guide for drilling operations in shale formations.

2. Experimental

2.1. Materials

The core samples used in this experiment were all collected from the 1st, 2nd and 3rd Sub-layers of the Qianfoya shale formation in the Puguang Gas Reservoir. The KCl polysulfonate drilling fluid system was prepared with the following formulation: 5% bentonite, 0.45% NaOH, 5% KCl, 0.5% encapsulating agent, 1% polymeric fluid loss reducer, 0.5% cellulose, 2% phenolic resin, 1% high-temperature resistant composite fluid loss reducer, 2% sulfonated asphalt, 2% natural asphalt, 5% ultrafine calcium carbonate, and barite as the weighting agent. All chemical reagents for the drilling fluid were supplied by the oilfield, and deionized water was used as the solvent for preparing the test fluids.

2.2. Experimental Methods

2.2.1. Characterization of Shale Composition, Structure and Wetting Properties

As shown in Figure 1, shale property was characterized for hydro-mechanical coupling wellbore stability analysis. Before X-ray diffraction testing, the rock powder samples were crushed, ground, and sieved through a 300-mesh sieve. The clay mineral composition of the shale, including the types, relative contents and crystal structure characteristics of clay minerals, was determined using a fully automatic powder X-ray diffractometer (d/max-2500pc, manufactured by Rigaku Corporation, Japan). During the test, the prepared rock powder samples were evenly spread on a sample stage, and the diffraction test was carried out under the optimal working parameters: the scanning range was 3~60° (2θ), the scanning speed was 5°/min, and the step size was 0.02°. The diffraction data obtained from the test were analyzed to accurately identify the clay mineral composition of the shale.

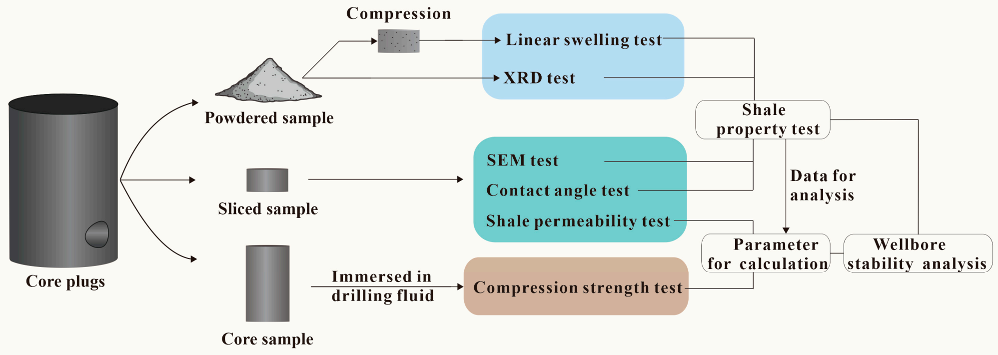

Figure 1. Flowchart for experimental test.

The mesoscale structure of the sliced shale sample was observed and analyzed using a scanning electron microscope (SU8220, produced by Hitachi Corporation, Tokyo, Japan) to clarify the microscopic morphology, pore structure, and mineral particle arrangement of the shale [32]. Prior to observation, the sliced shale samples were processed by vacuum drying to remove moisture in the pores, and then sprayed with a thin layer of gold film using an ion sputter coater to enhance the electrical conductivity of the sample surface, avoiding charge accumulation during the electron beam scanning process which would affect the observation effect. During the test, the accelerating voltage was adjusted within 5~20 kV according to the observation area and magnification, and the mesoscale structure characteristics of the shale sample were observed and recorded at different magnifications.

The contact angle of deionized water on the rock surface was measured with a contact angle analyzer (OCA20, manufactured by Dataphysics Corporation, Filderstadt, Germany), which was used to evaluate the wettability of the rock surface [33,34]. Before the test, the rock surface was polished and cleaned to remove surface pollutants and irregularities, ensuring that the test surface was smooth and flat. Then, the rock sample was fixed on the sample stage of the analyzer, and a micro-syringe was used to drop a 5 μL deionized water droplet onto the rock surface. The analyzer automatically captured the image of the water droplet on the rock surface and calculated the contact angle value using the Young–Laplace equation [34].

2.2.2. Linear Swelling Rate Test

The linear expansion rate of shale was determined via a shale swelling tester (NP-01, Qingdao Chuangmeng Technology Co., Ltd., Qingdao, China) using compacted powder samples (Figure 1). First, 15 g of core powder was ground, sieved through a 100-mesh sieve, dried at 105 °C for 4 h, and then cooled to room temperature. The powder was subsequently placed into a cylindrical core pressing mold with a 1-inch inner diameter and compacted under a pressure of 4 MPa for 5 min. The prepared core sample was put in the test cell, and an axial displacement measuring rod was centered on the sample surface and connected to a displacement sensor. After zeroing the sensor, distilled water was injected into the test cell; the axial expansion displacement was recorded in real time, and the corresponding expansion strain was calculated therefrom.

2.2.3. Shale Permeability and Compression Strength Test

A triaxial rock mechanics-permeability test system (THMC-I, Sichuan Huakongli Equipment Co., Ltd., Sichuan, China) was applied to determine the permeability and uniaxial compressive strength of rock specimens. The permeability of the mud cake and rock was measured via the pressure transmission method and the experimental setup was presented in Figure 2. First, a shale core was placed into the core holder, and the whole setup was heated to the reservoir temperature of 85 °C. Then, a confining pressure of 5.0 MPa was applied to the core. The upstream and downstream pore fluid pipelines were filled with a 5% KCl solution at a pressure of 1.0 MPa, and the downstream valve was closed upon achieving saturation equilibrium. The upstream pressure was then increased to 2.0 MPa, and the variations in downstream pressure were recorded throughout the process. After completing the shale pressure transmission test, the upstream fluid was replaced with drilling fluid while the downstream fluid remained the 5% KCl solution. Both the upstream and downstream fluids were pressurized to 1.0 MPa, followed by the closure of the downstream valve. The upstream pressure was raised to 2.0 MPa again, and the downstream pressure changes were recorded to calculate the permeability of the mud cake.

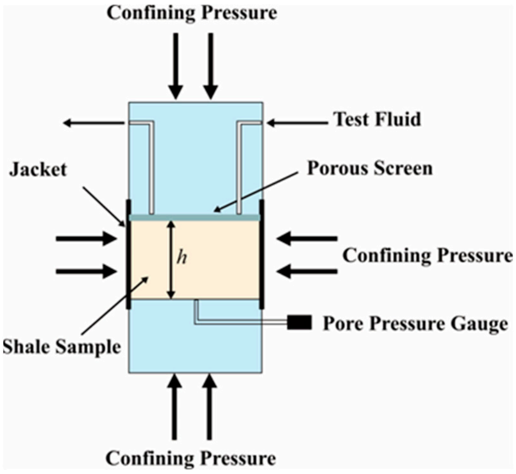

Figure 2. Experimental setup for shale and mud cake permeability test.

Shale strength was determined via a triaxial testing system. Core samples with dimensions of 1 inch in diameter × 2 inches in height were immersed in a water-based drilling fluid at 85 °C for 10 days. After immersion, the uniaxial compressive strength (UCS) was tested at a loading rate of 0.001 mm/s, and triaxial compression tests were conducted under a confining pressure of 5.0 MPa. Based on the Coulomb–Mohr failure criterion, the cohesive strength of the shale was subsequently derived from the strength data obtained under different confining pressure conditions.

https://doi.org/10.3390/pr14061002

3. Coupling Model for Wellbore Stability Analysis

3.1. Stress Distribution Around Wellbore

Wellbore stress distribution for inclined well can be calculated as [1,35],

$$\begin{aligned}
\sigma_{rr} &= \left(1-\tfrac{a^2}{r^2}\right)\tfrac{\sigma_{xx}}{2}+\left(1-4\tfrac{a^2}{r^2}+3\tfrac{a^4}{r^4}\right)\tfrac{\sigma_{xx}}{2}\cos 2\theta+\left(1-\tfrac{a^2}{r^2}\right)\tfrac{\sigma_{yy}}{2} \\
&\quad -\left(1-4\tfrac{a^2}{r^2}+3\tfrac{a^4}{r^4}\right)\tfrac{\sigma_{yy}}{2}\cos 2\theta+\left(1-4\tfrac{a^2}{r^2}+3\tfrac{a^4}{r^4}\right)\sigma_{xy}\sin 2\theta+\tfrac{a^2}{r^2}P_w \\
\sigma_{\theta\theta} &= \left(1+\tfrac{a^2}{r^2}\right)\tfrac{\sigma_{xx}}{2}-\left(1+3\tfrac{a^4}{r^4}\right)\tfrac{\sigma_{xx}}{2}\cos 2\theta+\left(1+\tfrac{a^2}{r^2}\right)\tfrac{\sigma_{yy}}{2}+\left(1+3\tfrac{a^4}{r^4}\right)\tfrac{\sigma_{yy}}{2}\cos 2\theta \\
&\quad -\left(1+3\tfrac{a^4}{r^4}\right)\sigma_{xy}\sin 2\theta-\tfrac{a^2}{r^2}P_w \\
\sigma_{r\theta} &= -\left(1+2\tfrac{a^2}{r^2}-3\tfrac{a^4}{r^4}\right)\tfrac{\sigma_{xx}}{2}\sin 2\theta-\left(1+2\tfrac{a^2}{r^2}-3\tfrac{a^4}{r^4}\right)\tfrac{\sigma_{yy}}{2}\sin 2\theta \\
&\quad +\left(1+2\tfrac{a^2}{r^2}-3\tfrac{a^4}{r^4}\right)\sigma_{xy}\cos 2\theta \\
\sigma_{zz} &= \sigma_{zz}^{i}-\nu\left(2\left(\sigma_{xx}-\sigma_{yy}\right)\tfrac{a^2}{r^2}\cos 2\theta+4\sigma_{xy}\tfrac{a^2}{r^2}\sin 2\theta\right) \\
\sigma_{rz} &= \sigma_{xz}\left(1-\tfrac{a^2}{r^2}\right)\cos\theta+\sigma_{yz}\left(1-\tfrac{a^2}{r^2}\right)\sin\theta \\
\sigma_{\theta z} &= \sigma_{yz}\left(1+\tfrac{a^2}{r^2}\right)\cos\theta-\sigma_{xz}\left(1+\tfrac{a^2}{r^2}\right)\sin\theta
\end{aligned} \tag{1}$$

where σ represents the stress around the wellbore, and the subscript represents the direction of stress. x, y, z represent the x, y, z directions in three-dimensional coordinates, r, θ, z represent the radial, circumferential, and vertical directions in polar coordinates, σ_{ii} represents the normal stress in the corresponding direction, and σ_{ij} represents the shear stress in the corresponding direction.

The relationship between the stress in three-dimensional coordinates and the maximum horizontal principal stress σ_H, minimum horizontal principal stress σ_h, and overlying rock pressure σ_v is as follows:

$$\begin{bmatrix} \sigma_{xx} \\ \sigma_{yy} \\ \sigma_{zz} \\ \sigma_{xy} \\ \sigma_{yz} \\ \sigma_{xz} \end{bmatrix} = \begin{bmatrix} \cos^2 d_w \cos^2 i_w & \sin^2 d_w \cos^2 i_w & \sin^2 i_w \\ \sin^2 d_w & \cos^2 d_w & 0 \\ \cos^2 d_w \sin^2 i_w & \sin^2 d_w \sin^2 i_w & \cos^2 i_w \\ -\sin d_w \cos d_w \cos i_w & \sin d_w \cos d_w \cos i_w & 0 \\ -\sin d_w \cos d_w \sin i_w & \sin d_w \cos d_w \sin i_w & 0 \\ \cos^2 d_w \sin i_w \cos i_w & \sin^2 d_w \sin i_w \cos i_w & -\sin i_w \cos i_w \end{bmatrix} \begin{bmatrix} \sigma_H \\ \sigma_h \\ \sigma_v \end{bmatrix} \tag{2}$$

where i_w represents the inclination angle and d_w represents the azimuth angle. The principal stress at the wellbore can be calculated as,

$$\begin{aligned}
\sigma_1 &= p_w \\
\sigma_2 &= \tfrac{\sigma_{rr}+\sigma_{\theta\theta}}{2}+\sqrt{\left(\tfrac{\sigma_{rr}-\sigma_{\theta\theta}}{2}\right)+\sigma_{r\theta}^2} \\
\sigma_3 &= \tfrac{\sigma_{rr}-\sigma_{\theta\theta}}{2}+\sqrt{\left(\tfrac{\sigma_{rr}-\sigma_{\theta\theta}}{2}\right)+\sigma_{r\theta}^2}
\end{aligned} \tag{3}$$

The maximum principal stress was the maximum of σ_1, σ_2 and σ_3, while the minimum principal stress was the minimum of σ_1, σ_2 and σ_3.

3.2. Continuity Equation for Fluid Flow in Mud Cake and Shale

Figure 3 shows the pore pressure distribution during drilling fluid filtration from wellbore to mud cake and the matrix. It is assumed that fluid flow in both the shale and mud cake follows Darcy's law, with gravity effects neglected, and that the fluid is single-phase and incompressible. Incorporating Darcy's Law, the general form of the continuity equation for fluid flow in a mud cake can be expressed as follows [27]:

$$\frac{\alpha\varphi}{K_f}\dot{p} - \frac{k_c}{\eta}\nabla^2 p = 0 \tag{4}$$

where K_f is fluid bulk modulus, MPa, φ is shale porosity, α is the ratio of mud cake porosity over shale porosity, k_c is mud cake permeability, μm^2, and η is fluid viscosity, mPa·s.

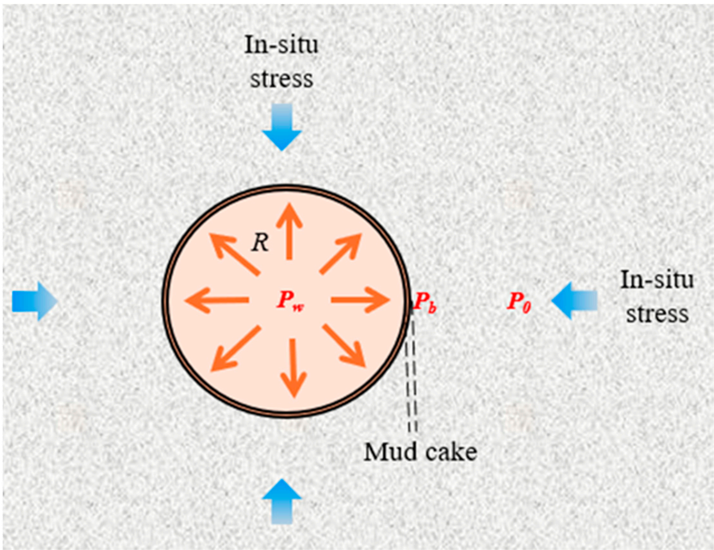

Figure 3. Filtration from drilling fluid through mud cake to wellbore.

The continuity equation for fluid flow in shale can be expressed as [27]:

$$\frac{1 - K/K_s - \varphi}{K_s}\dot{p} - \frac{k_{sh}}{\eta}\nabla^2 p = 0 \tag{5}$$

where K is rock bulk modulus, MPa, K_s is rock skeleton bulk modulus, MPa, and k_{sh} is shale permeability, μm^2.

Around the wellbore, the boundary conditions were,

$$\mathrm{r} \le \mathrm{R}\text{: } p = p_w;\ \mathrm{r} = \mathrm{R} + \mathrm{d},\ \frac{k_{sh}}{\mu}\left(\frac{\partial p}{\partial x}\right)_{sh} = \frac{k_b}{\mu}\left(\frac{\partial p}{\partial x}\right)_b;\ \mathrm{r} = \infty,\ p = p_0$$

where r was distance from the center of wellbore, R was radius, and d was the thickness of mud cake. p_w, p_b, p_0 were the wellbore pressure, the pore pressure at the wellbore, and the pore pressure of formation, respectively.

Combining the boundary conditions and Equations (4) and (5), p_b can be obtained.

3.3. Calculation of Safe Drilling Mud Density

The Coulomb–Mohr failure criterion is widely adopted to judge shear failure, which can be expressed as [1–4,27]:

$$(\sigma_1 - \sigma_3) - (\sigma_1 + \sigma_3)sin\varphi = 2Ccos\varphi \tag{6}$$

The tensile strength failure criterion can be expressed as [1–4,27]:

$$\sigma_3 = -\sigma_t \tag{7}$$

In the formula, σt represents the rock tensile strength.

By solving Equations (4) and (5) via finite element method, the pore pressure at the wellbore wall can be derived. On this basis, the stress distribution and principal stresses at the wellbore wall are calculated using Equations (1)–(3). The Mohr–Coulomb rock failure criterion is adopted to judge the occurrence of shear failure, while Equation (7) is applied to identify tensile failure. The detailed solution procedure is illustrated in Figure 4.

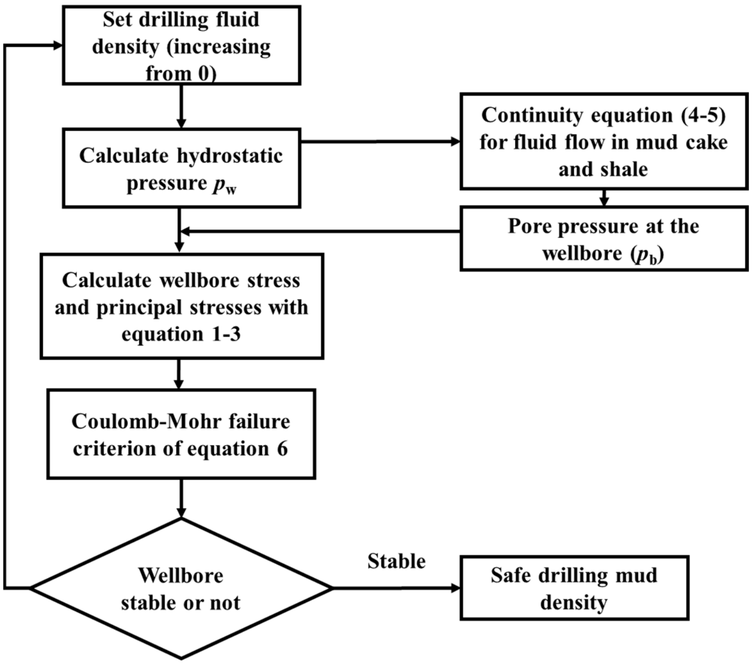

Figure 4. Calculation process of the safe mud density window.

4. Results and Discussion

4.1. Shale Mineral Composition

As shown in Figure 5, the shale is dominated by quartz, plagioclase and clay minerals as its main mineral components. Among the three Sub-layers, the third Sub-layer has the highest quartz content, while clay mineral abundances vary distinctly across the Sub-layers: the first Sub-layer features the highest clay mineral content at 35.50%, which is dominated by chlorite and illite; the second Sub-layer has the second-highest clay mineral content at 32.31%, with chlorite as the primary constituent; and the third Sub-layer contains the lowest clay mineral content at 18.78%, mainly composed of illite.

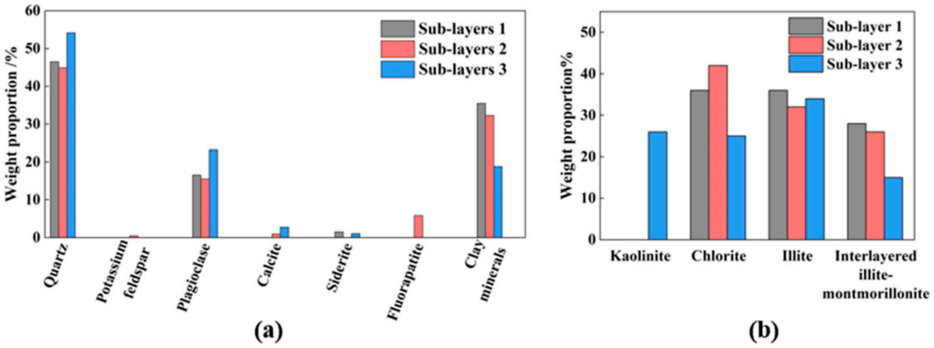

Figure 5. Mineral composition (**a**) and clay mineral components (**b**) of shale.

4.2. SEM Test

Figure 6 presents the mesoscale structure of shale samples in the three Sub-layers. The rock sample from Sub-layer 1 is dominated by argillaceous material, sand-grade clastics and calcareous components, exhibiting a silty mud texture with a shale structure. Its argillaceous material is composed of cryptocrystalline to fine scaly particles with random distribution, and partial aggregates show a striated arrangement. The rock sample from Sub-layer 2 features the same major constituents (argillaceous material, sand-grade clastics and calcareous components), yet it has a sandy mud texture with a pseudo-shale structure. The morphological and distribution characteristics of its argillaceous material are consistent with those of Sub-layer 1, consisting of cryptocrystalline to fine scaly particles in random distribution and partial striated aggregates. The rock sample from Sub-layer 3 is composed of sand-grade clastics and interstitial material. The sand-grade clastics, dominated by feldspar, quartz and rock fragments, are subangular and randomly distributed; the rock fragments include claystone, siliceous rock and clay-siliceous rock, with visible mica debris interspersed [33].

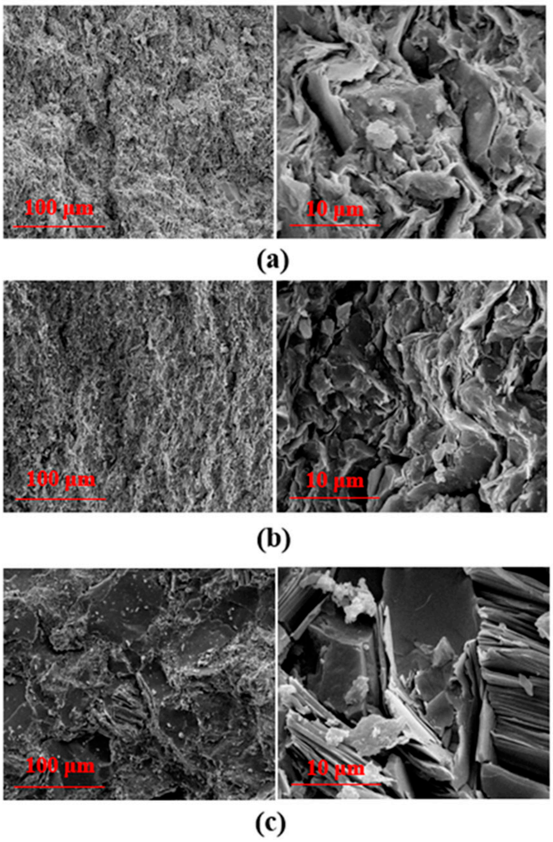

Figure 6. The surface SEM pictures of shale sample from Sub-layer 1 (**a**), from Sub-layer 2 (**b**), and that from Sub-layer 3 (**c**).

4.3. Rock Contact Angle Test

The water contact angles on the rock surfaces were measured, with the results presented in Figure 7. The measured water contact angles of samples from Sub-layers 1, 2, and 3 were 47.00°, 45.50°, and 24.50°, respectively. The shale sample from Sub-layer 1 exhibited lower hydrophilicity than that from Sub-layer 2, whereas the sample from Sub-layer 3 showed the strongest hydrophilicity.

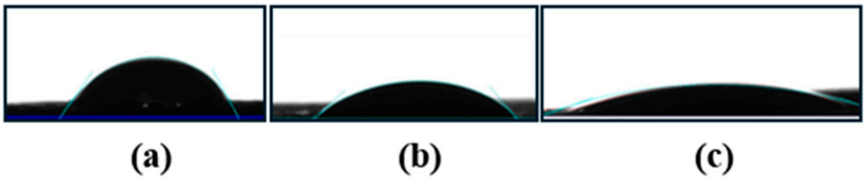

Figure 7. Contact angle of water on surface of shale samples from Sub-layer 1 (**a**), from Sub-layer 2 (**b**), and that from Sub-layer 3 (**c**).

4.4. Linear Swelling Test

The results of the linear swelling strain test are presented in Figure 8, which show that the sample from Sub-layer 2 had the highest hydration expansion rate, reaching 5.79% after equilibration. In contrast, the core sample from Sub-layer 3 exhibited the lowest expansion rate (1.28% post-equilibration), and that from Sub-layer 1 was 3.89%.

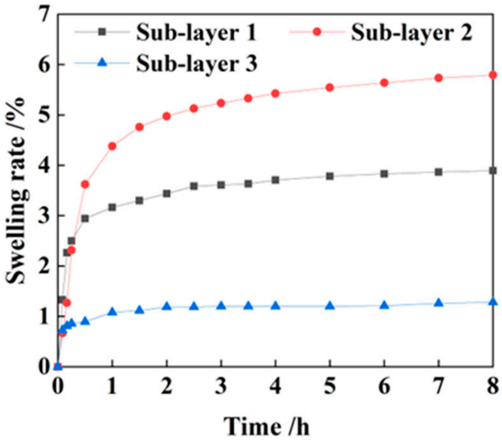

Figure 8. Linear swelling test results of shale samples.

4.5. Shale and Mud Cake Permeability Calculation

In the shale pore pressure transmission test, the boundary conditions were [34],

$$\mathrm{x} = 0\text{:}\ \ p = p_{up};\ \mathrm{x} = \mathrm{L}\text{:}\ \frac{k_{sh}\partial p}{\mu \partial x} = \frac{V\beta}{A}\frac{\partial p}{\partial t}$$

where x was distance from surface of upper end and L was height of shale core slices. Combining the boundary conditions and Equation (4), pressure change in downstream pressure can be calculated numerically. The shale permeability was achieved by validating the calculated data with the fluid flow model against the pore pressure transmission test data. On the other hand, the permeability can also be obtained analytically with Equation (8) [15,36,37].

$$\frac{P_{(l,t)} - P_0}{P_m - P_0} = 1 - \exp(-\lambda) \rightarrow k = \frac{\lambda \mu \beta V l}{At} \tag{8}$$

where P(l,t) is downstream fluid pressure, MPa; Pm is the upstream fluid pressure, MPa; A is cross-section area of core, cm^2; k is the permeability, $\mu\mathrm{m}^2$; μ is fluid viscosity, mPa·s; β is fluid compressibility; V is the downstream fluid volume, cm^3; and l is the length of the rock, cm. By comparing the numerical and analytical results, the method was validated.

With the drilling fluid as upstream fluid, the boundary conditions for shale pore pressure transmission test were [35]:

$$\mathrm{x} = 0,\ p = p_{up};\ \mathrm{x} = \mathrm{d},\ \frac{k_{sh}}{\mu}\left(\frac{\partial p}{\partial x}\right)_{sh} = \frac{k_b}{\mu}\left(\frac{\partial p}{\partial x}\right)_b;\ \mathrm{x} = \mathrm{d} + \mathrm{h}\text{:}\ \frac{k_{sh}\partial p}{\mu \partial x} = \frac{V\beta}{A}\frac{\partial p}{\partial t}$$

where d was thickness of mud cake and h was the height of shale core. Combining the boundary conditions and Equations (4) and (5) [38], pressure change in downstream pressure can be calculated. By the trial-and-error approach method, as shown in Figure 9, the shale and mud cake permeability were achieved by validating the calculated data with the fluid flow model against the pore pressure transmission test data [39,40].

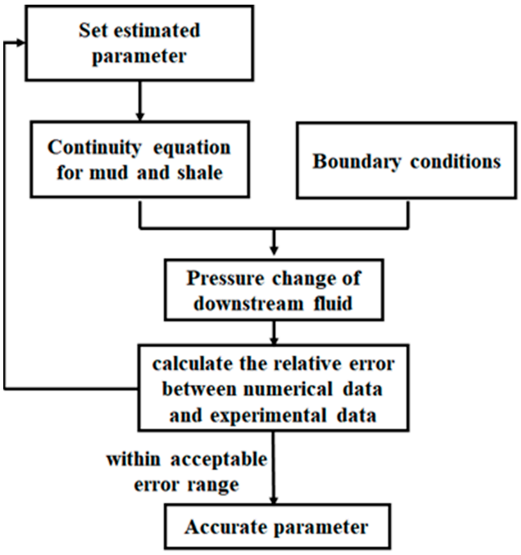

Figure 9. Flowchart to obtain shale and mud cake permeability.

The experimental results and corresponding fitting curves are presented in Figure 10. By numerically fitting the pressure change data, permeability for the rock matrix in Sub-layer 1 exhibits the highest values of 8.27×10^{-18} m^2 while that of Sub-layer 2 is 3.59×10^{-19} m^2, and Sub-layer 3 shows the lowest permeability of 2.76×10^{-20} m^2. On the other hand, by analytically fitting, permeabilities are 8.28×10^{-18} m^2, 3.58×10^{-19} m^2, 2.79×10^{-20} m^2, respectively, for the rock matrix in Sub-layer 1, Sub-layer 2, and Sub-layer 3. Compared to the analytical results, the errors of numerical values are all less than 1%, indicating high accuracy of the method [41–43]. The results reveal that mud cake for Sub-layer 1 exhibits the highest permeability of 2.07×10^{-20} m^2. By contrast, the permeability of the mud cake in Sub-layer 2 is 1.80×10^{-21} m^2 and that from Sub-layer 3 reaches the lowest value of 1.66×10^{-22} m^2. In terms of mud cake thickness, samples from Sub-layers 1 and 2 have a consistent thickness of 2.5 mm, whereas that from Sub-layer 3 features a thicker mud cake at 3.0 mm.

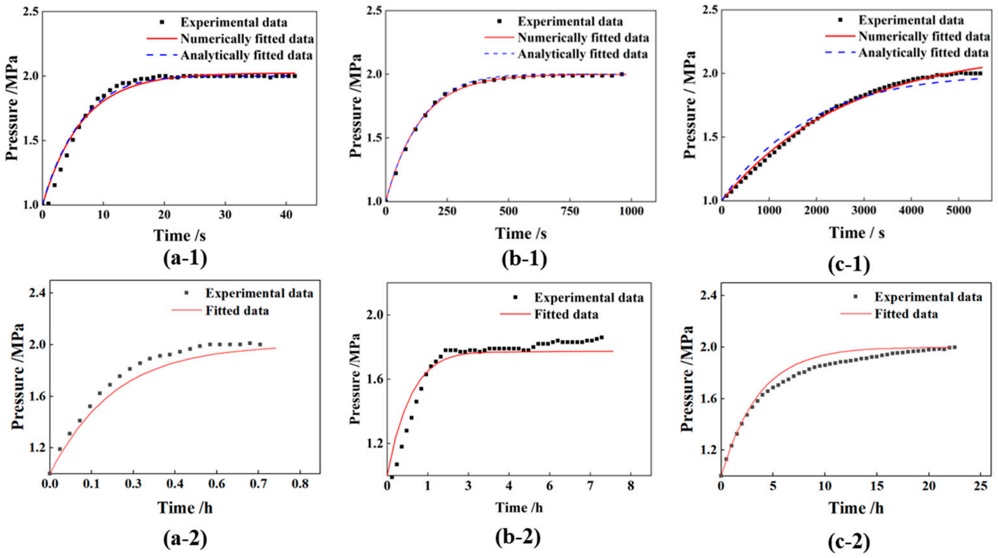

(a-1) (b-1) (c-1)
(a-2) (b-2) (c-2)

Figure 10. Experimental and fitted curve of downstream pressure change for shale samples with water solution as upstream test solution (Sub-layer 1 (**a-1**), Sub-layer 2 (**b-1**), and Sub-layer 3 (**c-1**)), and those with drilling fluid as the upstream test solution (Sub-layer 1 (**a-2**), Sub-layer 2 (**b-2**), and Sub-layer 3 (**c-2**)), respectively.

4.6. Uniaxial Compression and Cohesion Strength Before and After Immersion in Drilling Fluid

Figure 11 presents the uniaxial compressive strength of rock samples from different Sub-layers before and after 10 days of immersion in a water-based drilling fluid. Without drilling fluid immersion, the sample from Sub-layer 3 achieved the highest compressive strength of 141.47 MPa with a cohesion strength of 35.54 MPa; after immersion, its compressive strength and cohesion decreased to 130.40 MPa and 33.49 MPa, respectively. For the Sub-layer 1 sample, the compressive strength was 122.06 MPa prior to immersion and dropped to 64.21 MPa post-immersion, while its cohesion strength reduced from 27.16 MPa to 14.30 MPa, representing a decrease of 47.35%. The Sub-layer 2 sample had the lowest initial compressive strength at 77.42 MPa, which declined to 50.97 MPa after immersion; its cohesion strength decreased from 18.04 MPa to 10.46 MPa, with a reduction rate of 42.01%. In summary, the Sub-layer 1 sample suffered the most severe hydration damage, and the Sub-layer 2 sample exhibited the lowest strength after hydration.

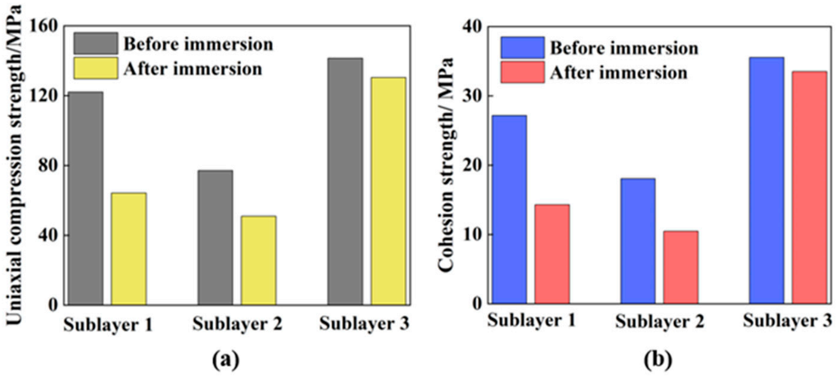

Figure 11. Uniaxial compression strength (**a**) and cohesion strength (**b**) before and after immersion in drilling fluid.

4.7. Calculation of Safe Drilling Mud Density Window

With the parameters shown in Table 1, pore pressure at the wellbore and safe drilling mud density window was calculated (Figure 12).

Table 1. Basic parameters and test parameters of shale formation.

Basic Parameter	Value	Test Parameter	Value	Test Parameter	Value
Well vertical depth	2487.50 m	Mud cake thickness in Sub-layer 1	2.5 mm	Cohesion strength of shale in Sub-layer 1 after immersion	14.30 MPa
Azimuth i_w	162.13°	Shale permeability in Sub-layer 1	8.27×10^{-18} m^2	Cohesion strength of shale in Sub-layer 2 after immersion	10.46 MPa
Inclination Angle i_w	86.84°	Mud cake permeability in Sub-layer 1	2.07×10^{-20} m^2	Cohesion strength of shale in Sub-layer 3 after immersion	33.49 MPa
Overburden stress σ_v	71.37 MPa	Mud cake thickness in Sub-layer 2	2.5 mm		
Maximum horizontal stress σ_H	62.05 MPa	Shale permeability in Sub-layer 2	3.59×10^{-19} m^2		
Minimum horizontal stress σ_h	55.16 MPa	Mud cake permeability in Sub-layer 2	1.80×10^{-21} m^2		
Pore pressure	34.15 MPa	Mud cake thickness in Sub-layer 3	3.0 mm		
Poisson's Ratio ν	0.22	Shale permeability in Sub-layer 3	2.76×10^{-20} m^2		
Bulk modulus K	38.85 GPa	Mud cake permeability in Sub-layer 3	1.66×10^{-22} m^2		

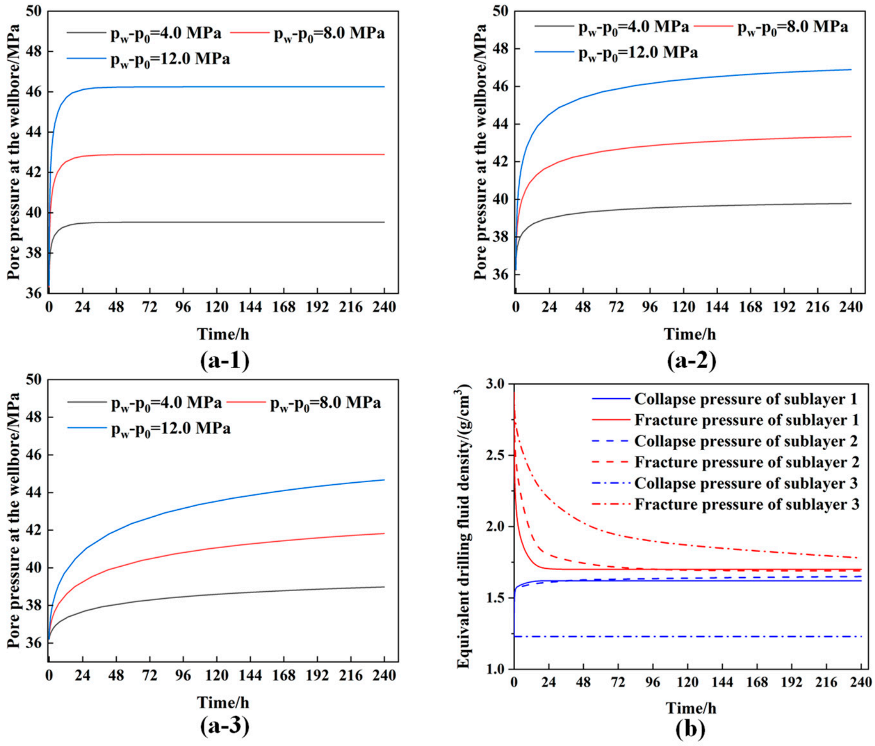

Figure 12. Pore pressure at the wellbore for Sub-layer 1 (**a-1**), Sub-layer 2 (**a-2**), Sub-layer 3 (**a-3**) and collapse pressure or fracture pressure for Sub-layers (**b**).

Wellbore pore pressure was calculated via the continuity equation, incorporating the permeability of the mud cake and shale (Figure 12(a-1–a-3)). Given that the samples from Sub-layer 3 exhibited the lowest permeability, pore pressure transmission was delayed, with the wellbore pressure increasing by 8.49 MPa, 5.64 MPa, and 2.80 MPa over 10 days under drilling fluid-pore pressure differentials of 12.0 MPa, 8.0 MPa, and 4.0 MPa, respectively. In contrast, samples from Sub-layer 1 had the highest permeability, with the wellbore pressure rising by 10.07 MPa, 6.71 MPa, and 3.36 MPa within the same 10-day period. Notably, the wellbore pressure of Sub-layer 1 increased sharply in the early stage, reaching 9.93 MPa, 6.62 MPa, and 3.30 MPa after just 1 day—values that were nearly identical to those measured at 10 days. The mud cake exerted a more pronounced delaying effect on wellbore pore pressure in Sub-layer 2 than in Sub-layer 1.

The collapse pressure and fracture pressure of Layers 1, 2, and 3 were derived, as illustrated in Figure 12b. The variation in fracture pressure was dominated by pore pressure evolution [44], which was determined by mud cake permeability and shale permeability. In the initial stage, as mud cake permeability increased, pore pressure transmission was enhanced [45,46], leading to a reduction in fracture pressure. At 1 h, the fracture pressure values were 2.84, 2.68, and 2.46 g/cm^3 for Layer 3 (lowest permeability), Layer 2 (medium permeability), and Layer 1 (highest permeability), respectively. On the other hand, the collapse pressure was dependent on both pore pressure evolution and the cohesion strength of shale [47]. At time = 0 (without pore pressure transmission), the pore pressure remained at its initial value for all three layers, and the collapse pressure increased as the cohesive strength decreased. Cohesion strength after immersion for Layer 3, Layer 1, and Layer 2 were 33.49 MPa, 14.30 MPa, 10.46 MPa with corresponding collapse pressure being 123, 1.53, and 1.55 g/cm^3, respectively. As pore fluid filtrated from the drilling mud into the shale formations, the buildup of pore pressure led to a rise in collapse pressure. For Layer 1 and Layer 2, the collapse pressure increased by 0.11 g/cm^3 and 0.10 g/cm^3, respectively. In contrast, the collapse pressure of Layer 3 was lower than the in situ pore pressure in the absence of pore fluid invasion, resulting in a nearly constant collapse pressure over time. Consequently, compared with pore pressure transmission, cohesive strength caused a more significant variation in collapse pressure. After 10 days, the mud density windows for Layer 1, Layer 2, and Layer 3 were determined as 1.62–1.70 g/cm^3, 1.65–1.69 g/cm^3, and 1.23–1.78 g/cm^3, respectively. Layer 2 exhibited the narrowest density window (0.04 g/cm^3), making it the most susceptible to wellbore stability failures. In conclusion, the safe mud density window of the target formation is relatively narrow, and the maintenance of wellbore stability requires strict control of the drilling mud density within the range of 1.65–1.69 g/cm^3.

5. Conclusions

The physicochemical properties of the shale were experimentally characterized, and the permeability of the filter cake and shale matrix was derived by fitting pressure transmission test data. On this basis, the safe drilling fluid density window for the formation was calculated. The main conclusions are drawn as follows:

(1) The clay content of this formation is as high as 35.5%. The average water contact angle of each Sub-layer is 39°, which indicates the strong hydrophilicity of the shale. Among them, Sub-layer 3 exhibits the strongest hydrophilicity with a contact angle of 24.5°, while Sub-layer 1 has the highest hydration swelling rate of 5.79%.

(2) Shale samples from Sub-layer 1 show the highest permeability for both the rock matrix and filter cake, at 8.27×10^{-18} m^2 and 2.07×10^{-20} m^2, respectively. This is followed by Sub-layer 2, with the rock matrix and filter cake permeability being 3.59×10^{-19} m^2 and 1.80×10^{-21} m^2. Sub-layer 3 has the lowest permeability values, at 2.76×10^{-20} m^2 (rock matrix) and 1.66×10^{-22} m^2 (filter cake). These results suggest that the filter cake formed on Sub-layer 1 has the poorest sealing performance. After immersion in drilling fluid, uniaxial compression tests show that the cohesion strength of Sub-layer 1, 2 and 3 samples is reduced by 47.35%, 42.01% and 5.77%, respectively. Notably, Sub-layer 2 has the minimum cohesion after suffering hydration damage induced by drilling fluid.

(3) Analysis of the safe drilling fluid density window via a coupled wellbore stability model reveals that the shale formation has a narrow safety margin. After 10 days of exposure, the safe density windows for Sub-layers 1, 2 and 3 are determined to be 1.62–1.70 g/cm^3, 1.65–1.69 g/cm^3 and 1.23–1.78 g/cm^3, respectively. To ensure the stability of the target formation during drilling, a recommended safe drilling fluid density window of 1.65–1.69 g/cm^3 is proposed.

This study provides a theoretical foundation for wellbore stability analysis by considering the mud cake seepage effect using a hydro-mechanical coupling model. However, for the hydration weakening effect of shale in drilling fluid, only strength reduction was incorporated into the model. In future work, a thermal-hydro-chemical-mechanical (THCM) model can be adopted to further improve the accuracy of collapse pressure and fracture pressure predictions.

Author Contributions: Conceptualization, Q.G. and Q.L.; Methodology, Q.G. and F.H.; Software, H.H.; Validation, Y.B., H.H. and J.L.; Formal analysis, J.Z.; Investigation, S.J. and J.L.; Resources, S.J.; Data curation, S.J. and F.H.; Writing—original draft, Y.B. and J.L.; Writing—review and editing, J.Z.; Visualization, S.W.; Supervision, S.W. and Q.L.; Project administration, F.H. and Q.L. All authors have read and agreed to the published version of the manuscript.

Funding: This research received no external funding.

Data Availability Statement: The original contributions presented in this study are included in the article. Further inquiries can be directed to the corresponding author.

Conflicts of Interest: The authors declare no conflicts of interest.

References

1. Liu, H.; Cui, S.; Meng, Y.; Li, Z.; Yu, X.; Sun, H.; Zhou, Y.; Luo, Y. Rock mechanics and wellbore stability of deep shale during drilling and completion processes. *J. Pet. Sci. Eng.* **2021**, *205*, 108882. [CrossRef]
2. Li, Y.; Weijermars, R. Wellbore stability analysis in transverse isotropic shales with anisotropic failure criteria. *J. Pet. Sci. Eng.* **2019**, *176*, 982–993. [CrossRef]
3. Ding, Y.; Liu, X.; Liang, L.; Xiong, J.; Li, W.; Wei, X.; Duan, X.; Hou, L. Wellbore stability model in shale formation under the synergistic effect of stress unloading-hydration. *Petrol. Explor. Dev.* **2023**, *50*, 1478–1486. [CrossRef]
4. Gao, X.; Wang, M.; Shi, X.; Dai, P.; Zhang, M. Wellbore stability research based on transversely isotropic strength criteria in shale formation. *Soils Found.* **2024**, *64*, 101541. [CrossRef]
5. Xu, K.; Liu, Z.; Chen, Q.; Zhang, Q.; Ling, X.; Cai, X.; He, Q.; Yang, M. Application of machine learning in wellbore stability prediction: A review. *Geoenergy Sci. Eng.* **2024**, *232*, 212409. [CrossRef]
6. Hu, Y.; Yang, Y. A Comparative Study on Drag Reduction Methods for Continental Shale Drilling in the Fuxing Block, Southeastern Sichuan Basin. *Reserv. Sci.* **2026**, *2*, 81–96. [CrossRef]
7. Li, Q.; Li, Q.; Wu, J.; Li, X.; Li, H.; Cheng, Y. Wellhead stability during development process of hydrate reservoir in the Northern South China Sea: Evolution and mechanism. *Processes* **2024**, *13*, 40. [CrossRef]
8. Suo, Y.; Dong, M.; Fu, X.; He, W.; Pan, Z. Experimental and numerical simulation research on hot dry rock wellbore stability under different cooling methods. *Geothermics* **2024**, *119*, 102977. [CrossRef]
9. Yang, Y.; Huang, F.; Kang, S. Mechanism of Penetration Rate Improvement in Hot Dry Rock Under the Coupling of Impact Load and Confining Pressure Release. *Reserv. Sci.* **2026**, *2*, 52–64. [CrossRef]
10. Shan, Y.; Xue, Q.; Wang, J.; Li, Y.; Wang, C. Analysis of the influence of downhole drill string vibration on wellbore stability. *Machines* **2023**, *11*, 762. [CrossRef]
11. Tran, M.H.; Abousleiman, Y.N.; Nguyen, V.X. The effects of filter-cake buildup and time-dependent properties on the stability of inclined wellbores. *SPE J.* **2011**, *16*, 1010–1028. [CrossRef]
12. Fang, C.; Wang, Q.; Jiang, H.; Chen, Z.; Wang, Y.; Zhai, W.; Chen, S. Shale wellbore stability and well trajectory optimization: A case study from Changning, Sichuan, China. *Pet. Sci. Technol.* **2023**, *41*, 564–585. [CrossRef]
13. Li, J.; Qiu, Z.; Zhong, H.; Zhao, X.; Liu, Z.; Huang, W. Effects of water-based drilling fluid on properties of mud cake and wellbore stability. *J. Pet. Sci. Eng.* **2022**, *208*, 109704. [CrossRef]
14. Gao, C.; Miska, S.Z.; Yu, M.; Ozbayoglu, E.M.; Takach, N.E. Effective enhancement of wellbore stability in shales with new families of nanoparticles. In *SPE Deepwater Drilling and Completions Conference*; Paper No. D012S018R003; SPE: Richardson, TX, USA, 2016. [CrossRef]
15. Zhang, H.; Yao, J.; Zhang, S.; Chen, H. Carboxylized graphene oxide nanosheet for shale plugging at high temperature. *Appl. Surf. Sci.* **2021**, *558*, 149901. [CrossRef]
16. Cui, X.; Wang, C.; Huang, W.; Zhang, S.; Chen, H.; Wu, B. Composite of carboxylized graphene oxide with nanosilica for shale plugging. *J. Phys. Chem. Solids* **2025**, *200*, 112574. [CrossRef]
17. Meng, X.; Huang, X.; Sun, J.; Lv, K.; Li, H.; Wang, Z.; Yuan, Z. Ultra-high temperature resistant polystyrene/acrylic resin microspheres for enhanced wellbore stability of oil-based drilling fluids. *Colloids Surf. A Physicochem. Eng. Asp.* **2025**, *725*, 137637. [CrossRef]
18. Liu, Y.F.; Zhou, L.; Wan, X.C.; Tang, Y.F.; Liu, Q.; Li, W.; Liao, J.B. Synthesis and Characterization of a Temperature-Sensitive Microcapsule Gelling Agent for High-Temperature Acid Release. *ACS Omega* **2024**, *9*, 20849–20858. [CrossRef]
19. Xu, N.; Wang, Y. Effect of Nanomaterials on Improving the Apparent Viscosity of Heavy Oil and the Environmental Evaluation of Reservoir Environment. *Reserv. Sci.* **2026**, *2*, 1–15. [CrossRef]
20. Zhang, Q.; Jia, W.; Fan, X.; Liang, Y.; Yang, Y. A review of the shale wellbore stability mechanism based on mechanical–chemical coupling theories. *Petroleum* **2015**, *1*, 91–96. [CrossRef]
21. Shokir, E.M.; Sallam, S.; Abdelhafiz, M.M. Comprehensive wellbore stability modeling by integrating poroelastic, thermal, and chemical effects with advanced numerical techniques. *ACS Omega* **2024**, *9*, 51536–51553. [CrossRef]
22. Chenevert, M.E.; Dewan, J.T. A model for filtration of water-base mud during drilling: Determination of mudcake parameters. *Petrophysics* **2001**, *42*, 237–250.
23. Feng, Y.; Li, X.; Gray, K.E. An easy-to-implement numerical method for quantifying time-dependent mudcake effects on near-wellbore stresses. *J. Pet. Sci. Eng.* **2018**, *164*, 501–514. [CrossRef]
24. Feng, Y.; Li, X.; Gray, K.E. Mudcake effects on wellbore stress and fracture initiation pressure and implications for wellbore strengthening. *Pet. Sci.* **2018**, *15*, 319–334. [CrossRef]
25. Cao, L.; Lv, M.; Li, C.; Sun, Q.; Wu, M.; Xu, C.; Dou, J. Effects of crosslinking agents and reservoir conditions on the propagation of fractures in coal reservoirs during hydraulic fracturing. *Reserv. Sci.* **2025**, *1*, 36–51. [CrossRef]

26. Li, X.; Jaffal, H.; Feng, Y.; Mohtar, C.E.L.; Gray, K.E. Wellbore breakouts: Mohr-Coulomb plastic rock deformation, fluid seepage, and time-dependent mudcake buildup. *J. Nat. Gas Sci. Eng.* **2018**, *52*, 515–528. [CrossRef]
27. Zhang, S.; Wang, H.; Qiu, Z.; Cao, W.; Huang, H.; Chen, Z. Calculation of safe drilling mud density window for shale formation by considering chemo-poro-mechanical coupling effect. *Petrol. Explor. Dev.* **2019**, *46*, 1271–1280. [CrossRef]
28. Wan, L.; Gao, H.; Zhang, S.; Cui, X.; Chen, H.; Xing, Q.; Zhu, Y. Effects of fluid flow in triple porosity medium on fracture width and its propagation during lost circulation control. *Geoenergy Sci. Eng.* **2023**, *230*, 212281. [CrossRef]
29. Zhang, S.; Li, J.; Wang, H.; Huang, H.; Wang, C.; Cui, X.; Huang, W.; Wan, L. Mechanisms of lost circulation induced fracture propagation and fracture width prediction in shale reservoirs. *Nat. Gas Ind.* **2025**, *45*, 121–132.
30. Gao, S.Y.; Bo, K.H.; Zhang, Y.Y.; Gao, H.; Huangpu, J.L. Study on wellbore instability mechanism of continental shale reservoir in Northeastern Sichuan Basin. *Drill. Complet. Fluid* **2025**, *42*, 217–224.
31. Bo, K.H.; Gao, S.Y.; Jin, Y.; Chen, J.H. Study on hydration damage characteristics of continental shale with multi-type weak planes in Qianfoya Formation, Puguang Area. *Pet. Sci. Bull.* **2025**, *10*, 496–510.
32. Tahir, M.U.; Guo, S. Preliminary Investigation of Fracture Behavior during Carbon Dioxide Fracturing of Natural Hydrogen Reservoir with Hard-Core Imperfections. *Reserv. Sci.* **2026**, *2*, 34–51. [CrossRef]
33. Ali, J.; Ansari, U.; Ali, F.; Javed, T.; Hullio, I.A. Application of Machine Learning for Effective Screening of Enhanced Oil Recovery Methods. *Reserv. Sci.* **2026**, *2*, 65–80. [CrossRef]
34. Yang, X.; Shang, Z.; Shi, Y.; Peng, Y.; Yue, Y.; Chen, S.; Jiang, G.; Cai, J. Influence of salt solutions on the permeability, membrane efficiency and wettability of the Lower Silurian Longmaxi shale in Xiushan, Southwest China. *Appl. Clay Sci.* **2018**, *158*, 83–93. [CrossRef]
35. Liu, C.; Han, Y.; Phan, D.T.; Abousleiman, Y.N. Stress solutions for short-and long-term wellbore stability analysis. *J. Nat. Gas Sci. Eng.* **2022**, *105*, 104693. [CrossRef]
36. Zhang, S.; Sheng, J.J. Effect of water imbibition on hydration induced fracture and permeability of shale cores. *J. Nat. Gas Sci. Eng.* **2017**, *45*, 726–737. [CrossRef]
37. Li, W.; Liao, J. Microscopic Analysis of Flow Resistance of Oil Displacement Fluid in Reservoir Fractures. *Reserv. Sci.* **2026**, *2*, 16–33. [CrossRef]
38. Ounegh, A.; Hasan-Zadeh, A.; Khanaposhtani, M.M.; Kazaemzadeh, Y. Wellbore stability analysis based on the combination of geomechanical and petrophysical studies. *Results Eng.* **2024**, *24*, 103016. [CrossRef]
39. Jamshidi, E.; Kianoush, P.; Hosseini, N.; Adib, A. Scaling-up dynamic elastic logs to pseudo-static elastic moduli of rocks using a wellbore stability analysis approach in the Marun oilfield, SW Iran. *Sci. Rep.* **2024**, *14*, 19094. [CrossRef]
40. Wei, Y.; Feng, Y.; Tan, Z.; Yang, T.; Yan, S.; Li, X.; Deng, J. Simultaneously improving ROP and maintaining wellbore stability in shale gas well: A case study of Luzhou shale gas reservoirs. *Rock Mech. Bull.* **2024**, *3*, 100124. [CrossRef]
41. Li, M.; Liu, J.; Xia, Y. Risk prediction of gas hydrate formation in the wellbore and subsea gathering system of deep-water turbidite reservoirs: Case analysis from the south China Sea. *Reserv. Sci.* **2025**, *1*, 52–72. [CrossRef]
42. Lu, Y.; Li, W.; Jin, Y.; Chen, M.; Pang, H.; Zhou, W. Short-and long-term wellbore stability analysis for a horizontal well in a transversely isotropic poroelastic formation. *Rock Mech. Rock Eng.* **2025**, *58*, 767–786. [CrossRef]
43. Motahari, M.; Hashemi, A.; Molaghab, A. Successful mechanical earth model construction and wellbore stability analysis using elastic and plasticity solutions, a case study. *Geomech. Energy Environ.* **2022**, *32*, 100357. [CrossRef]
44. Liu, C.; Phan, D.T.; Abousleiman, Y.N. The implication of time-dependent filter cake buildup on wellbore stability and breakdown pressure. *Rock Mech. Rock Eng.* **2025**, *58*, 1529–1547. [CrossRef]
45. Wu, J.; Ansari, U. From CO_2 Sequestration to Hydrogen Storage: Further Utilization of Depleted Gas Reservoirs. *Reserv. Sci.* **2025**, *1*, 19–35. [CrossRef]
46. Liu, H.; Cui, S.; Meng, Y.; Chen, Z.; Sun, H. Study on mechanical properties and wellbore stability of deep sandstone rock based on variable parameter MC criterion. *Geoenergy Sci. Eng.* **2023**, *224*, 211609. [CrossRef]
47. Li, H.; Sun, J.; Lv, K.; Huang, X.; Zhang, P.; Zhang, Z. Wettability alteration to maintain wellbore stability of shale formation using hydrophobic nanoparticles. *Colloids Surf. A Physicochem. Eng. Asp.* **2022**, *635*, 128015. [CrossRef]

https://doi.org/10.3390/pr14061002